Infrared Light Emission from Semiconductor Devices

Daniel L. Barton, Paiboon Tangyunyong, Jerry M. Soden, and Alan Y. Liang
Sandia National Laboratories
Electronics Quality/Reliability Center
P.O. Box 5800, MS 1081
Albuquerque, NM 87185-1081
Frank J. Low and Alexander N. Zaplatin
Infrared Laboratories, Inc.
1808 East 17th Street
Tucson, AZ 85719-6505
Kandiah Shivanandan
Institute of Microelectronics, NUS
11 Science Park Rd., Science Park II, Singapore 0511
Republic of Singapore
Gregory Donohoe
The University of New Mexico
Albuquerque, NM

Abstract

We present results using near-infrared (NIR) cameras to study emission characteristics of common defect classes for integrated circuits (ICs). The cameras are based on a liquid nitrogen cooled HgCdTe imaging array with high quantum efficiency and very low read noise. The array was developed for infrared astronomy and has high quantum efficiency in the wavelength range from 0.8 to 2.5 μm. For comparison, the same set of samples used to characterize the performance of the NIR camera were studied using a non-intensified, liquid-nitrogen-cooled, slow scan CCD camera (with a spectral range from 400-1100 nm). Our results show that the NIR camera images all of the defect classes studied here with much shorter integration times than the cooled CCD, suggesting that photon emission beyond 1 μm is significantly stronger than at shorter wavelengths.

LIGHT (OR PHOTON) EMISSION MICROSCOPY is a common failure analysis technique for semiconductor devices. The considerations involved in using photon emission to successfully analyze defects and failure mechanisms in CMOS ICs are well known [1,2]. IC analysis has typically been performed by collecting visible (390 - 770 nm) and some near infrared (770 - 1000 nm, with the NIR band defined as 770 - 1500 nm) wavelength photons emitted from transistors, *pn* junctions, and other photon-generating structures on or near the top (front), electrically-active, silicon surface. These photons are transmitted through the overlying, relatively transparent dielectric layers, passing between or scattered around the patterned, opaque metal interconnections. Detection of photons that emerge from around these overlying layers is referred to as frontside light emission analysis. Correspondingly, imaging light passing through the silicon substrate and emerging from the bottom (back) is referred to as backside light emission analysis.

Custom and commercial systems are routinely used for light emission analysis. The spectral characteristics for these systems are usually dependent upon the type of detector chosen. Most commercial systems use detectors based on image intensifiers or CCD arrays. Although some companies provide detectors with extended NIR capability for backside analysis, most systems have very low response to photons with wavelengths beyond 1 μm.

There is increasing interest in backside light emission analysis. This is driven primarily by the advancement of IC fabrication technologies with additional opaque conductor layers and packaging technologies that place the active side of the die down in close proximity to the package. Backside analysis takes advantage of silicon's transmission of photons with energies less than its indirect silicon bandgap energy, corresponding to wavelengths greater than 1.107 μm (for undoped silicon). It is commonly known that silicon becomes less transparent as dopants are added. Because of this, the heavily doped substrates often used with newer technologies will attenuate NIR light emitted from the active circuits. These factors and others are stimulating research for solutions, including improved substrate thinning techniques, increased NIR imaging sensitivity, and spectral analysis.

It is well known that different types of photon emission processes can be distinguished by their spectra. While radiative recombination emission from silicon structures is generally centered around 1.1 μm (plus or minus a phonon), most defect-related emission is strongest in the NIR range as will be demonstrated in this study. Commonly used cameras have spectral responses centered in the 400 - 900 nm range and can thus capture only a small portion of the emitted light.

MASTER

DISCLAIMER

Portions of this document may be illegible
in electronic image products. Images are
produced from the best available original
document.

Theory of Light Emission from Silicon ICs

In order to better understand the nature of the emission spectra from various processes in silicon devices, a general treatment of emission from indirect gap semiconductors is presented. Although a detailed section on this subject would be insightful, the complexity and detail required to cover the material is beyond the scope of this paper.

General recombination processes in semiconductors can be broken down into two main categories: interband and intraband.

Radiative interband transitions occur when an electron in an excited state (occupying a state in the conduction band for example) recombines with a hole (or empty state) in a lower energy band (a hole in the valence band for example) to emit a photon. In indirect gap semiconductors such as silicon, this process must be accompanied by the emission or the absorption of a phonon as illustrated by the energy band diagram in Fig. 1(a). Because of the relative lack of phonons for absorption at room temperature, this process is usually dominated by phonon emission. This means that, for indirect materials, there will be a significant amount of radiative emission at energies that are a phonon (or a combination of phonons) less than the bandgap or at slightly longer wavelengths. Additional spectral content can come from recombination involving impurity energy levels, both donors (P at $E = E_C - 0.045$ eV and As at $E = E_C - 0.054$ eV) and acceptors (B at $E = E_V + 0.045$ eV) which can further reduce the emitted photon energy and thus push the emission wavelength farther into the IR range as illustrated in Fig. 1(b). Hot electrons (or holes) which carry energy $kT_e = \Delta E$, represent the only major component by which light at energies significantly greater than the indirect bandgap can be emitted.

Intraband recombination, as the name implies, occurs when an excited electron recombines with a vacant state in the same band. Usually, this process will not lead to a photon of significant energy for defect detection purposes but it could conceivably contribute if the energy of the excited electron is more than 1 eV or so above the conduction (or below the valence) band edge. This type of emission is a component in the continuum commonly found in light emission spectra.

Photon emission from defects or abnormal operation of silicon microelectronic devices generally falls into only a few of the possible categories: forward or reverse biased *pn* junctions, transistors in saturation, latchup, and gate oxide breakdown.

Forward biased *pn* junctions have perhaps the easiest photon emission mechanism to understand. The mechanism is very similar to that of light emitting diodes (LEDs) and semiconductor lasers. The emission of these devices is generated by placing a large population of electrons and holes in close physical proximity where they recombine. This generates light with spectra centered around the bandgap. Usually, because this is a low voltage emission mechanism, there will be very few highly energetic carriers and thus the

photon emission will not extend significantly toward shorter wavelengths. An example of this process found in a very early, but highly referenced article [4], is shown in Fig. 2. Fig. 2 shows the emission spectra for both forward and reverse (which will be described below) biased *pn* junctions.
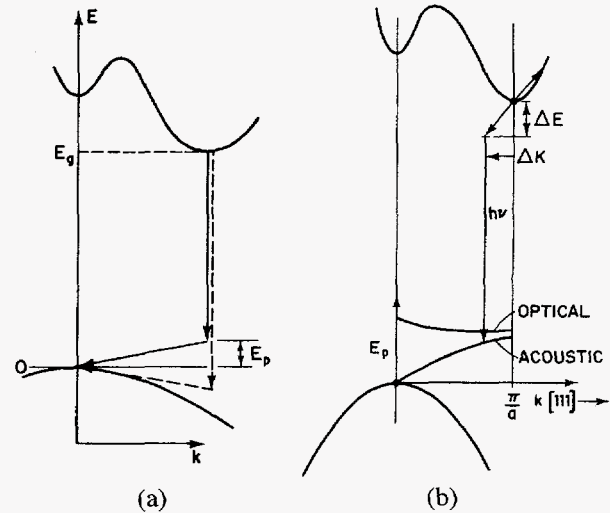

(a)   (b)

Fig. 1 - Energy band diagrams for indirect transitions (a) Phonon assisted transitions (b) Impurity and/or hot electron ($kT_e = \Delta E$) assisted [3]

Reverse biased *pn* junctions represent a different situation. When a small reverse bias is applied to a junction, the depletion region widens, causing low current but a substantial electric field. As the reverse bias is increased, the probability that a highly excited electron will cross the junction increases. This will generate photons from the recombination of carriers whose energies can be significantly above the bandgap energy. The resulting emission spectrum will have a significant tail which can extend into the visible wavelengths. If the reverse bias is increased to the point of avalanche breakdown, the added emission from charge multiplication will dramatically increase the visible photon intensity as well. Although there can be a significant amount of visible light emission, the peak intensity of the emission spectrum will be near the indirect bandgap. The second curve in Fig. 2 shows a spectrum of a reverse biased *pn* junction. Fig. 2 shows that even though there is a tail at shorter wavelengths, the NIR emission component has the highest intensity.

A significant group of IC failure modes are the result of MOSFETs in saturation, including certain open and short circuits of metal or polysilicon interconnections [1,5-7]. Detection of emission from saturated transistors has been successful for *n*-channel MOSFETs but difficult for *p*-channel devices because of their much lower emission intensity.

To understand this emission process, the emission source must be considered. In a MOSFET, a gate voltage above the threshold voltage will create an inversion layer (a conductive channel) between the transistor's source and drain. If the voltage on the drain of the transistor is increased, the

depletion layer around the drain will neutralize the inversion layer and pinch off the channel at the drain side. Charge flow between source and drain must now include a drift component as carriers cross the pinchoff region. Evidence has shown [1] that the light emission intensity is strongly coupled to the amount of substrate current. This indicates that the energetic carriers from the source or drain are radiatively recombining with majority carriers from the body of the MOSFET. Because this is similar to the reverse biased *pn* junction, the spectrum should be similar. Fig. 3 shows a spectrum obtained from an *n*-channel MOSFET in saturation [5]. The similarity to the reverse bias curve in Fig. 2 supports this hypothesis. The transistor in Fig. 2 was biased with $V_{DS} = V_{GS}/2$, a situation known to maximize substrate current and photon emission [1].
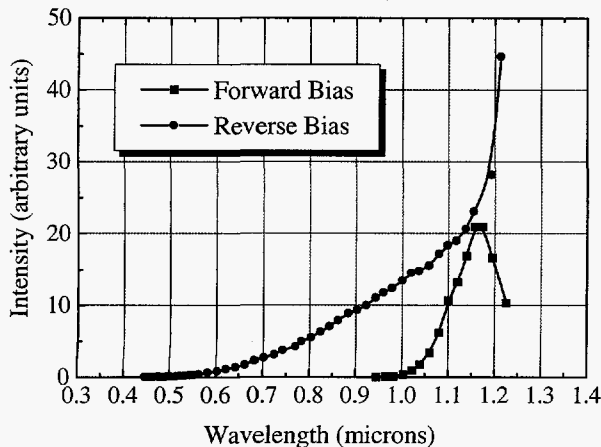
Fig. 2 - Measured spectra from forward and reverse biased Si, *pn* junctions[4]

While this process creates photons detectable with most commercial light emission systems, light emission from *p*-channel MOSFETs under the same conditions is more difficult to detect. This is due to ionization potential differences between electrons and holes, making emission from *p*-channel transistors significantly weaker. For *n*-channel transistors, as Fig. 3 demonstrates, the strongest emission is in the NIR range. Thus, to detect the weaker emission from *p*-channel transistors and thereby increase defect detection, an NIR detector is the optimal choice.

A third mechanism producing light emission is latchup. The classic model for latchup in CMOS ICs uses two parasitic bipolar transistors connected to form a silicon-controlled rectifier (SCR). When the SCR goes into its "ON" or low impedance state, all three of the SCR junctions are forward biased, placing the bipolar transistors in saturation. For these conditions, the expected emission spectrum will be of the same general shape shown in Fig. 2 for a forward biased *pn* junction. The difference in this case is the relative area occupied by the parasitic SCR in comparison to a single *pn* junction on the same IC and the resulting amount of current required by the circuit during latchup. These factors make imaging latchup events possible with a silicon CCD camera or an intensified camera by providing more emission at shorter

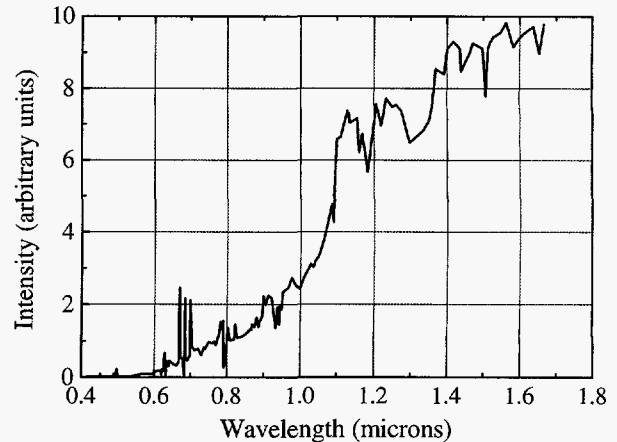wavelengths, but, at the same time, the NIR intensity is also much larger.

Fig. 3 - Measured spectrum from *n*-MOSFET saturation emission [8]

Perhaps the most difficult emission to explain is that of gate oxide shorts. This is a very common failure mechanism that is very difficult to locate without the use of light emission techniques. When gate oxide fails, a conductive path is created through the oxide. This connection is like a local alloy junction between the gate material, usually polycrystalline silicon, and the single crystal silicon in the channel region or in the source/drain region of the transistor. This situation would lead to an expected emission spectrum similar to those shown in Fig. 2. As will be shown later, measured spectra indicate that there is a strong component in the visible that decays in the NIR. This might indicate that the emission is thermionic, but the temperature needed to create a visible emission peak makes this unlikely. The exact emission process for gate oxide failures is not well understood.

Because of the recent popularity of flip-chip technologies and the rapid escalation in the number of metal interconnect layers which obscure the frontside view of transistors, the need for light emission technology for backside (through the silicon substrate) analysis has increased. As the previous sections indicate, there are strong signals from all of the main light emitting defect types in the NIR. To meet this need, both a sensitive detector and one with good quantum efficiency for wavelengths beyond 1 µm is needed. The subject of this paper is to demonstrate the use of such a camera and show that it is not only advantageous for backside analysis but is ideal for all light emission processes on silicon ICs.

Description of Samples

A number of samples were required to demonstrate both the spectra for different IC emission mechanisms and to provide a basis for comparison of visible and NIR camera technology.

To assure validity for state of the art CMOS technology, samples were obtained from the current 0.5 µm, 3-level metal CMOS process being used at Sandia National Laboratories.

Parts fabricated using this process are designed for 3.3 volt operation. Test structures containing *n*- and *p*-channel MOSFETs which had channel lengths from 0.5 μm to 20 μm and a common channel width of 20 μm were selected to study the emission processes from transistors in saturation. Several 256K SRAMs fabricated in this same technology were stressed using a human body model ESD test system to study the emission from ESD induced defects.

In order to study the emission from gate oxide shorts, it was decided to use failures that had previously been studied [9]. The ICs were SA3000s, Sandia's static CMOS version of the Intel 8085 8-bit microprocessor. These ICs were from a production lot that had a high gate oxide defect density. These ICs were used in a study on the reliability and electrical properties of gate oxide shorts. This study used elevated voltage and temperature stress to evaluate changes in quiescent power supply current (I_{DDQ}) and functional test behavior due to oxide breakdown and subsequent instability of the gate oxide short.

The backside sample was also obtained from a previous failure analysis investigation. The analysis of this sample has been previously published [10,11]. The samples are functional equivalents of an Intel 87C51 microcontrollers which were fabricated at Sandia in a radiation hardened, fully static 1.25 μm, 2-level metal CMOS technology. The original failure analysis had been performed on the front side of the die using the charge induced voltage alteration, CIVA, technique [10] which helped determine that a pellicle scratch had caused a lithography problem resulting in poor contact definition in one region. The same samples were analyzed from the backside again using the light-induced voltage alteration, LIVA, technique [11]. For this study, the availability of a backside sample which had both I/O ports (both *n*- and *p*-channel transistors) that could be placed in saturation as well as a failure site was ideal.

Image processing

To extract the light emission signal from the background noise, several different image processing techniques were used. The general method was to locate the signal area within the image, calculate the mean pixel value in that region, then find a representative non-signal area and calculate the mean in that area. The difference in the mean values is a measure of the signal level above the background. Once the signal level has been determined, it can be adjusted to compensate for filter transmission, exposure time, device current, etc. to allow accurate analyses to be performed.

For improved signal extraction, a spectral filter was used. Prior to calculating image statistics, the Crimmins geometric algorithm was used to smooth the data [12]. This algorithm is best understood by visualizing the image as a surface where a pixel gray scale value (temperature) defines a height above the surface. Features of interest ("signal") appear as tall, flat structures projecting from a level substrate, like mesas standing over the desert floor. Noise appears as local, random fluctuations in the height of the surface. In order to

make accurate statistical measures of the features, we need to devise a filter that will suppress the noise while preserving the features. The "signal" and "noise" so defined are not separable in the spatial frequency domain, and linear, space-invariant filters that suppress the noise invariably smear the signal. Nonlinear filters like the median filter [13] threaten to obliterate tall narrow features. The nonlinear Crimmins algorithm exploits the local properties of signal and noise. Each iteration of the algorithm examines a 3x3 pixel neighborhood and applies a series of minimum and maximum operators to reduce the local curvature. It is as if sharp projections of the surface were chipped away, and narrow holes filled in with the debris. Both the mesas and the noise are affected, but because the mesas are tall and the noise variations small, only a few iterations are sufficient to suppress the noise while leaving the mesas essentially intact.

Visible to NIR Light Emission

In order to provide a basis for comparison, the above samples were first studied using a non-intensified silicon CCD camera. The camera used was a liquid nitrogen-cooled, slow-scan camera with a thinned, back illuminated 512 by 512 pixel CCD array. The use of liquid nitrogen cooling effectively reduces the dark current noise to a negligible level, about two electrons per hour. The quantum efficiency (a measure of the detector's ability to collect light at a given wavelength) of this CCD array is shown in Fig. 4. Fig. 4 indicates that the peak in quantum efficiency is in the 600-700 nm wavelength band with a gradual drop in efficiency with increasing wavelength out to 1 μm. At 1 μm, the detector has a quantum efficiency of 17%. For longer wavelengths, the quantum efficiency drops quickly to only a few percent. The abrupt loss in quantum efficiency near the indirect bandgap of silicon is a direct consequence of the materials used to make the CCD array and demonstrates that silicon detectors may not be the best choice for imaging emission processes in silicon ICs. Although detectors of this type have been marketed in systems for backside light emission analysis, their low efficiency for wavelengths to which silicon is transparent severely limits what can be detected.
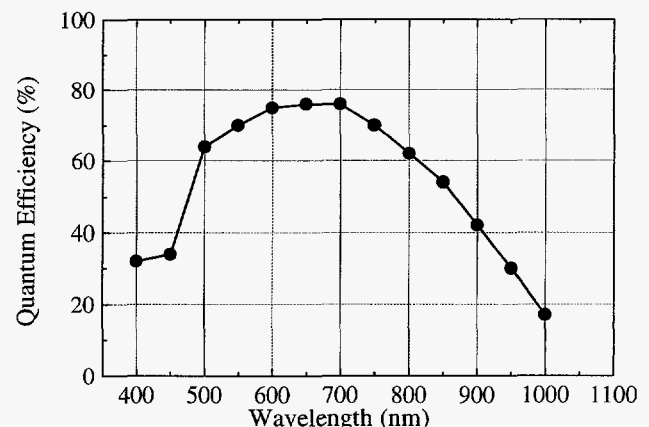

Fig. 4 - CCD array quantum efficiency vs. wavelength [14]

For comparison to the CCD array specifications, Fig. 5 shows the peak radiant sensitivity of several common image intensifiers [15] as a function of wavelength. Fig. 5 shows that even the GEN III - NIR intensifier will have limited applicability for the detection of light at energies near the silicon bandgap. These detectors rely on their ability to detect the relatively small amount of light in their spectral range of sensitivity.
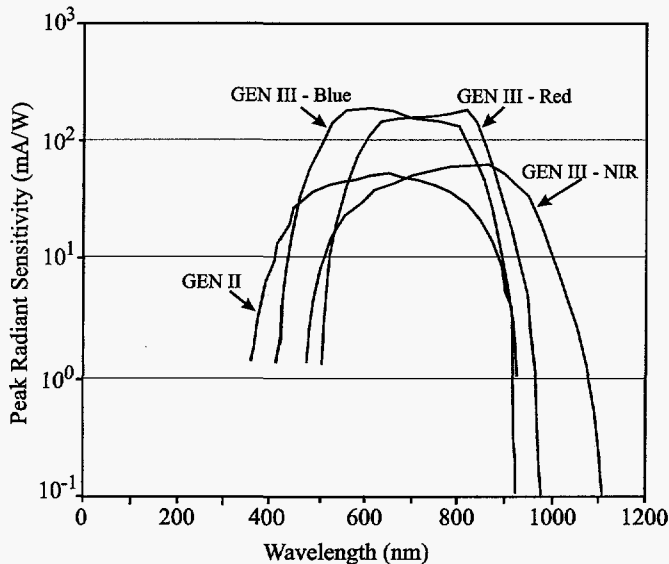

Fig. 5 - Spectral response of various image intensifiers [15]

The first samples analyzed with the cooled, silicon CCD array were those with gate oxide shorts. These samples had shorts in both p- and n-channel MOSFETs that were imaged at wavelengths from 400 to 1100 nm using a series of bandpass filters. Once the signal was extracted from the background noise, it was corrected for both the filter response and the CCD quantum efficiency. The typical exposure times needed to achieve sufficient signal-to-noise levels for each image ranged from as short as 5 seconds at wavelengths around 700 nm to over 300 seconds at 1100 nm. Since the sample was fabricated in an 11 V technology, a supply voltage of 11 V was used, resulting in an I_{DDQ} of 6.6 mA. The p- and n-channel gate short samples represent very strong emission sources. The resulting spectra are shown in Fig. 6. The data obtained is interesting because there is virtually no difference between the emission spectra for gate oxide shorts in p- and n-channel MOSFETs. This analysis suggests that the emission process is independent of the type of single crystal material to which contact has been made and indicates hot electron processes are responsible for the peak at visible wavelengths. A simple calculation using Wein's displacement law gives a corresponding temperature for a thermionic emission process of over 4800 K, which is clearly not physically possible for silicon ICs. Therefore the emission process must be dominated by electrons which have been excited to well above the conduction band edge radiatively recombining with vacant states in the valence band.
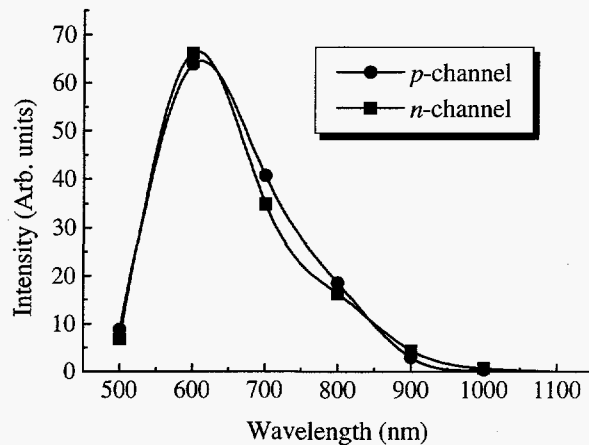

Fig. 6 - Comparison of spectra from gate oxide shorts in both n- and p-channel MOSFETs; note the similarity

The other process which was characterized using the CCD array was saturation current emission from n- and p-channel MOSFETs. For this test, several 0.5 and 0.6 μm channel length test transistors were biased with $V_{DS} = 3.3$ V and $V_{GS} = 1.65$ V in order to maximize the substrate current and thus maximize the light emission. The transistors were imaged using the same bandpass filters as were used for the gate oxide short samples. While the n-channel transistors were easily imaged using an integration time of 300 seconds, emission from the p-channel devices was so weak that no signal could be detected even after 1800 seconds of integration time. Fig. 7 shows the spectra obtained from n-channel devices of two different channel lengths and with two different microscope objectives. This data is consistent with the results shown in Fig. 3, except for the roll off in intensity at 1000 nm. The differences detected between the two objectives used indicate that the transmission of most microscope objectives is lower near 1000 nm and the quantum efficiency of the CCD array at the same wavelength may be
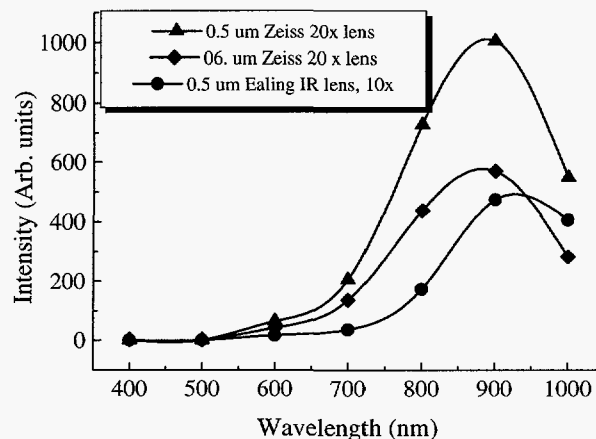

Fig. 7 - Comparison of spectra from n-channel MOSFETs of different channel lengths and using different microscope objectives

optimistic. The objective used for comparison (Ealing IR lens) was an infrared optimized reflecting objective with a 97% transmission efficiency between 0.95 µm and 10 µm and thus was not responsible for any additional transmission loss in the NIR.

For failure analysis applications bandpass filters normally are not used. Emission detection is normally done using the full spectral width of the detector to minimize integration time. Fig. 8 shows the imaging results from an *n*-channel MOSFET in saturation after 300 seconds integration time and Fig. 9 shows the corresponding *p*-channel images. Both emission images were taken using the full spectral range of the CCD camera system.
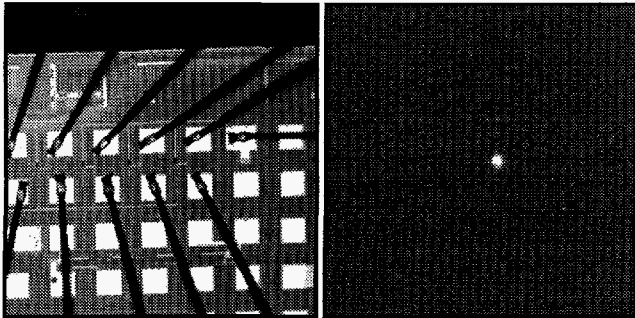
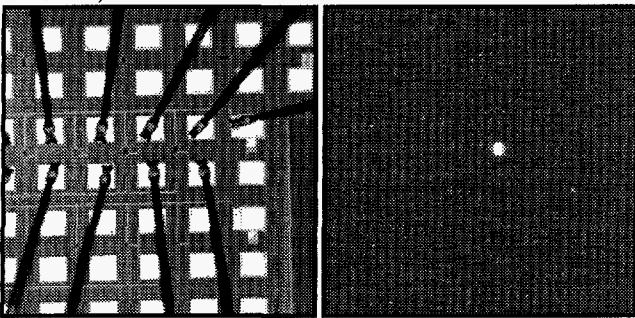Fig. 8 - *n*-channel (channel length = 0.5 µm) saturation current emission, t = 150 seconds

Fig. 9 - *p*-channel (channel length = 0.5 µm) saturation current emission, t = 900 seconds

For gate oxide short-related emission, images can be obtained in a matter of a few seconds. As was illustrated in Fig. 6, the peak in the spectra related to this particular emission type falls well within the high quantum efficiency wavelength range of CCD arrays. This makes gate oxide shorts easy to detect with visible wavelength detectors.

Near Infrared camera system

A 256x256 pixel HgCdTe NIR array developed for use on the Hubble Space Telescope was used to image in the 800 - 2500 nm band. This so called NICMOS-3 array was developed for NASA by Rockwell International and the Steward Observatory at the University of Arizona. The Near Infrared Camera Multi-Object Spectrograph (NICMOS) is scheduled for launch on the Shuttle in February 1997. The overall quantum efficiency of the system is listed in Table 1.

Table 1 - Quantum efficiency of NICMOS camera system

Wavelength (µm)	Quantum Efficiency (%)
0.8	cut-on
1.3	35
1.65	45
2.2	85
2.5	cut-off

The first prototype camera [16] developed for microscopic applications, now in use at The National University of Singapore (NUS), was designed to utilize the full spectral range of the detector from 800 to 2500 nm. This camera used a cooled, anti-reflection coated ZnSe window to provide good transmission between 500 nm and 5000 nm as well as low thermal emission. This camera incorporates a six position filter wheel cooled to 77 K and incorporates five wide bandpass filters whose center wavelengths and peak transmissions are listed in Table 2. This camera is mounted on a three axis Alessi probe station. This is believed to be the first IR microscope to utilize an NIR array with performance comparable to that of cooled CCD arrays.

Table 2 - IR filter transmission and center wavelengths

Center wavelength, λ_p (nm)	Transmission at λ_p (%)
870	85
1100	60
1250	60
1650	60
2200	60

The usual read noise of the NICMOS-3 array is 35 electrons but modifications using special read techniques can reduce this noise to less than 15 electrons. Because the temperature of the array is maintained near 77 K, the dark current is negligible for integration times from 100 milliseconds to greater than 100 seconds. Thus, it is possible to measure photon fluxes at the array of less than 1 photon per second. While experimental evidence suggests that the emission from IC related processes is still strong past 1400 nm, thermal background from the sample starts to become noticeable and limits the sensitivity to non-thermal emission. In order to eliminate thermal information, a cold filter which has a cutoff at 1400 nm and very low leakage at longer wavelengths can be placed in front of the array. The spectral response of this filter, which is referred to as a J-filter in astronomy, is shown in Fig. 10.

A second prototype camera system has been built to take advantage of these improvements and is in use at Infrared Laboratories. A schematic diagram of this camera's main components is shown in Fig. 11. An average quantum efficiency of 38% in the 1100 to 1400 nm band was measured on this camera. Except where noted, this camera was used to perform the NIR light emission analysis presented in this study.
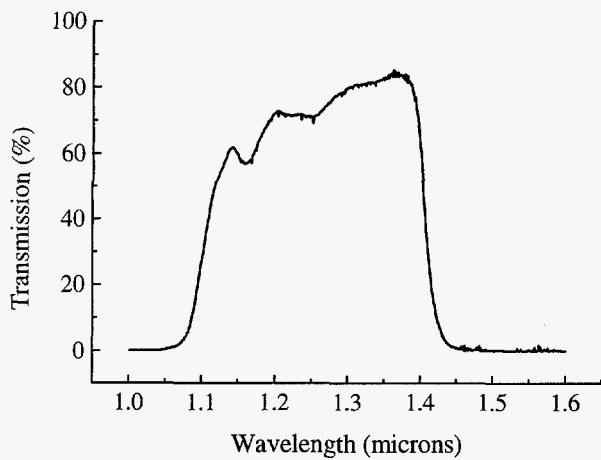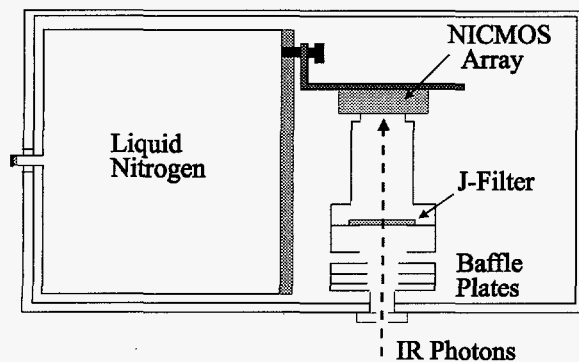
Fig. 10 - J-filter transmission characteristics

Fig. 11 - Layout of Infrared Laboratories camera setup optimized for 1100 to 1400 nm

Results from the NIR Cameras

From both the theory of light emission and the results presented for the Si CCD array camera, the light emission from the most common IC defects should be greater in the infrared than in the visible to near IR range (except possibly for the emission from gate oxide failures). To prove this point, the same samples analyzed with the Si CCD camera were analyzed with the NICMOS camera.

As was done with the CCD camera, both n- and p-channel MOSFETs were imaged in saturation. Both transistor types were biased at $V_{DS} = 3.3$ V, $V_{GS} = 1.65$ V which gave a nominal drain to source current of 1.94 mA for the n-channel and 1.2 mA for the p-channel transistors. In contrast to the CCD analysis, the emission from the p-channel transistors was strong enough to obtain high signal-to-noise data with a reasonable integration time. In fact, using the full 1.1 - 1.4 μm wavelength band of the J-filter, emission images could be acquired with less than 10 seconds integration time using the 0.5 μm channel length n- and p-channel transistors. For the spectral work where bandpass filters were placed in front of the J-filter, a 10 second integration time was used for the n-channel devices while a 30 second integration time was used for the p-channel devices. The results, which have been corrected for filter transmission, exposure time, and device

current, are shown in Fig. 12. As expected, the emission from the n-channel transistors is significantly stronger at all wavelengths, but the p-channel spectrum does maintain the same general characteristics. Both curves have a strong signal at 1.1 μm and a peak at around 1.3 μm (which is harder to see for the p-channel devices because of the vertical scale in the figure). The signal at 1.1 μm is undoubtedly from radiative recombination around the indirect bandgap of silicon. Because the spectra were obtained using discrete filters, no information about the peak width was available. For comparison, Fig. 13 shows the results obtained using the NICMOS camera at NUS over the wavelength range from 1.2 to 2.25 μm. The curves in Fig. 13 do not show a short wavelength rise indicating that the observed signal at 1.1 μm in Fig. 12 may be fairly narrow. It also should be noted that the presence of a strong signal at 1.1 μm contradicts the CCD camera results which indicated a drop in intensity. This contradiction is most likely due to an overestimation of the quantum efficiency of the CCD array even at 1.0 μm.

Since the signals were strong from both transistor types, data was also collected to measure the changes in signal intensity as a function of channel length (and thus electric field). As before, all transistors were biased at $V_{DS} = 3.3$ V, $V_{GS} = 1.65$ V. Fig. 14 shows the results of this analysis with no bandpass filters in the camera, only the J-filter. As expected, the data shows that the intensity of the light emission from saturation is inversely proportional to channel length.

The SRAM subjected to human body model ESD testing was also analyzed in the infrared. The example I/O structure showed evidence of a leaky protection diode (pn junction) after the ESD testing. With the IC biased at $V_{DD} = 3.3$ V, it drew a supply current of 5.23 mA. Emission from the damaged input was strong at 100 seconds integration time and was still detectable at 30 seconds. Since emission from this sample could also be detected in a commercial light emission system using an S1 type image intensifier in approximately 10 seconds, some of the damage to the sample may be gate oxide related.
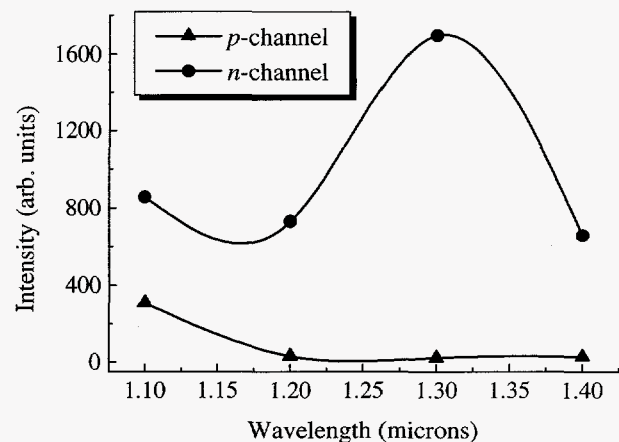

Fig. 12 - n- and p-channel saturation emission (1.1 to 1.4 μm)
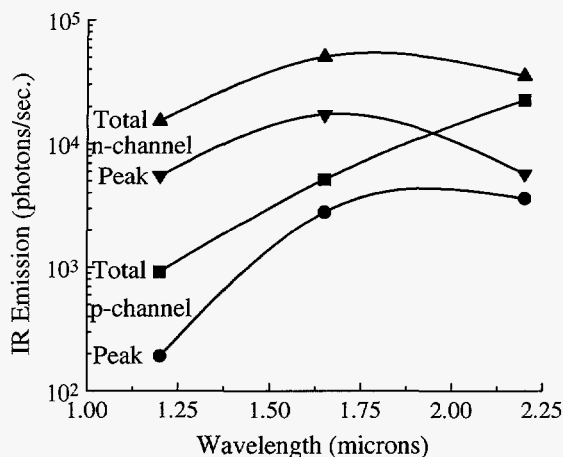
Fig. 13 - *n*- and *p*-channel saturation emission from 1.2 to 2.25 μm (log scale)

Light emission analysis from the die backside is perhaps the application where infrared cameras are unchallenged by other imaging technologies. To demonstrate this, the backside sample described earlier was analyzed. Fig. 15 shows both a reflected infrared image and the corresponding light emission image. The emission in this case was generated by placing one of the output buffer transistors in saturation by applying a voltage of 3.5 V to the output pin. This situation puts both the *n*-channel and the *p*-channel output buffer transistors into saturation since for both transistors, $V_{DS} > (V_{GS} - V_T)$. A power supply current of 225 μA at a voltage of 5.0 V was measured. The emission image in Fig. 15 was made using an exposure time of 10 seconds. Emission images were made with exposure times as short as 1.5 seconds.

The other important feature of this analysis is that no thinning of the substrate was required to reduce absorption. The sample was polished only enough to remove the eutectic die attach and create a smooth interface.
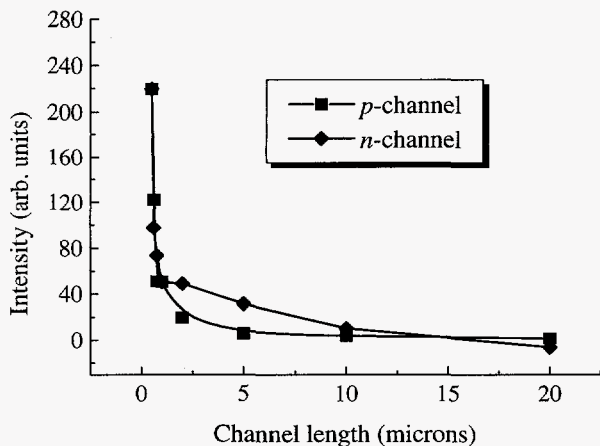

Fig. 14 - Comparison of spectra from *n*- and *p*-channel MOSFETs in saturation versus channel length over spectral range from 1.1 to 1.4 μm
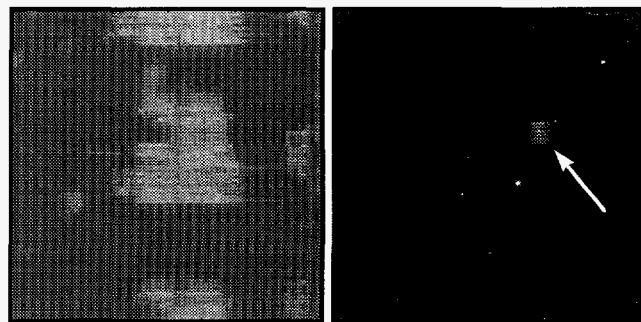

Fig. 15 - Infrared (1.1-1.4 μm) images of backside sample. Brightfield image (left) and emission image (right) after 10 sec. exposure. $V_{DD} = 3.5$ V, $I_{DD} = 0.225$ mA

The real challenge was to determine if there was enough emission from the defect area on this sample to be detected. As was found in an earlier study [10], the pellicle scratch created a problem with several contacts. The poorly defined contacts created a situation where several transistors could be placed in saturation. Fig. 16 shows both the defect area and the light emission collected after a 200 second integration time. The sample was biased at $V_{DD} = 5.0$ V yielding a current of 200 μA with the defect state active. It should be noted that the emission from this sample could not be detected with either a commercial light emission system with an S1 type image intensifier or the cooled CCD camera.
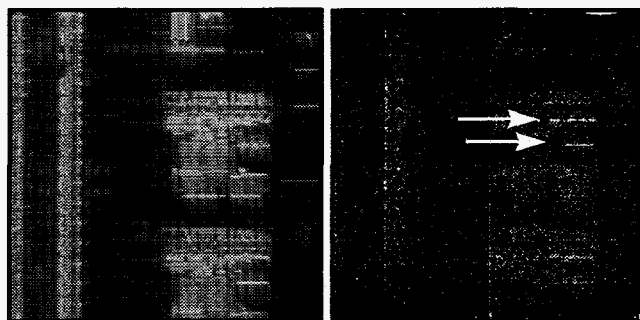

Fig. 16 - Infrared (1.1-1.4 μm) brightfield image (left) of defect area from a backside sample and corresponding emission image (right) after an exposure time of 200 seconds

The final series of samples analyzed were those with gate oxide shorts. As shown in Fig. 6, the emission from this class of defects exhibited a peak around 600 nm. This finding did create some concern about the potential for imaging their emission in the infrared. As it turned out, all concerns were premature as the emission was easily collected using very short exposure times (less than 1.5 seconds) using the NICMOS camera. Fig. 17 shows an example image collected using the full J-filter bandwidth with the sample biased at $V_{DD} = 6.0$ V and $I_{DD} = 1.47$ mA (remembering that this sample was manufactured for use at 11 V). While the spectral information shown in Fig. 6 for this same sample does contain a short wavelength peak, it is apparent that there is also a strong signal in the infrared, most likely at 1.1 μm, which is

easily detected by the infrared camera. This data shows that the gate oxide short class of defects is by far the easiest to detect.
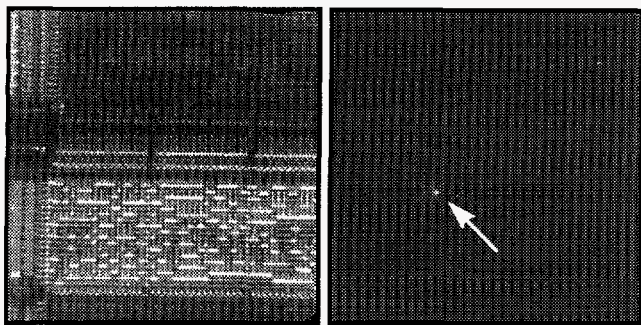

Fig. 17 - Infrared (1.1-1.4 μm) brightfield image (left) of gate oxide failure area and corresponding emission image (right) after an exposure time of 1.5 seconds

Conclusions

Careful analysis of the physics behind the different light emission processes from the most commonly encountered defect classes indicates there is a significant advantage in using the light emitted at wavelengths longer than 1 μm compared to shorter wavelengths. Published data supporting this analysis has been available for many years, but the detector technology suitable for detecting very weak NIR signals has only recently become mature enough for general application.

Data collected from the same samples using two different imaging technologies supports the need to image light emitting processes on silicon-based microelectronic devices in the infrared at wavelengths longer than 1 μm. The data collected on a sample prepared for backside analysis also demonstrates the utility of using a camera sensitive to longer wavelengths. The only samples encountered that might have shown that a visible camera would have better applicability were the gate oxide short samples. Images taken using the NIR camera proved that although there was a strong signal in the visible, a strong NIR signal was also present, allowing images to be collected with similar integration times. We estimate that images of similar signal-to-noise can be acquired using the NICMOS camera (1100 to 1400 nm band) with up to 1000 times shorter integration than the CCD camera (400 to 1100 nm band).

Acknowledgments

References

1 C. F. Hawkins, J. M. Soden, E. I. Cole Jr., and E. S. Snyder, Int. Symp. for Testing and Failure Analysis (ISTFA), pp. 55-67, Oct. 29-Nov. 2, 1990.

2 J. M. Soden and E. I. Cole, Jr., Tutorial, *Proc. Int. ReliabilityPhysics Symp.*, pp. 4a1-4a.16, Mar. 1992

3 J. I. Pankove, "Optical Processes in Semiconductors", ch. 6, Prentice-Hall, New Jersey (1971)

4 A. G. Chynoweth and K. G. McKay, Phys. Rev., 102 (2), 369-376 (1956)

5 J. M. Soden, R. K. Treece, M. R. Taylor, and C. F. Hawkins, *Proc. Int. Test Conf.*, pp. 423-430, Aug., 1989.

6 C.L. Henderson, J.M. Soden, and C.F. Hawkins, *Proc. Int. Test Conf.*, pp. 302-310, Oct., 1991.

7 C.F. Hawkins, J.M. Soden, A.W. Righter, and J. Ferguson, *Proc. Int. Test Conf.*, pp. 413-425, Oct., 1994.

8 A. Kux, P. Lugli, R. Ostermeir, F. Koch, and G. Deboy, Mat. Res. Soc. Symp. Proc., 256, 223-226 (1992)

9 C.F. Hawkins and J.M. Soden, *Proc. Int. Test Conf.*, pp. 443-451, Sept. 1986

10 E. I. Cole Jr. and J. M. Soden, Int. Symp. for Testing and Failure Analysis (ISTFA), pp. 1-8, 15-19 November, 1993

11 E. I. Cole Jr., J. M. Soden, J. L. Rife, D. L. Barton, and C. L. Henderson, *Proc. Int. ReliabilityPhysics Symp.*, pp. 388-398, 12-14 Apr. 1994

12 Crimmins, Thomas R, Applied Optics, 24 (10), 1438-1443 (1985)

13 Gonzalez, Rafael C., and Richard E. Woods, "Digital Image Processing", p. 191, Addison-Wesley (1992)

14 Data courtesy of A. L. Lichty, Photometrics, Inc.

15 Hypervision sales literature, (1996)

16 K. Shivanandan and K. Nyunt, Int. Symp. for Testing and Failure Analysis (ISTFA), pp. 69-71, 6-10 Nov., 1995